EDGE ARTICLE

Check for updates

Heavy-atom effect regulating room temperature phosphorescence in hybrid metal halide glasses

Linyuan Lian, Ming Ai, Daming Xiong, Tao Liang, Jibin Zhang, [ID] Mochen Jia, [ID] Ying Liu, Zhuangzhuang Ma, [ID] Xu Chen, [ID] Yanbing Han, [ID] Yongtao Tian, [ID] Xinjian Li and Zhifeng Shi [ID] *

Room-temperature phosphorescence (RTP) in hybrid metal halide glasses offers promising applications in optoelectronics and anti-counterfeiting, yet achieving tunable RTP properties remains challenging. Here, we report a solvent-assisted rapid evaporation method to synthesize a series of zero-dimensional (0D) butyltriphenylphosphonium-based (BuTPP$^+$) hybrid metal halide glasses with the composition (BuTPP)$_2$MCl$_2$X$_2$ (M = Zn, Cd; X = Cl, Br, I). By incorporating optically inert heavy-atom-containing metal halide units [MCl$_2$X$_2$]$^{2-}$, we demonstrate precise regulation of RTP lifetimes *via* the heavy-atom effect, with lifetimes decreasing from 608.6 ms for (BuTPP)$_2$ZnCl$_4$ to 146 ms for (BuTPP)$_2$CdCl$_2$Br$_2$ as the atomic number of inorganic metal halide units increases. Notably, when the atomic number exceeds 170 (*e.g.*, [ZnCl$_2$I$_2$]$^{2-}$ and [CdCl$_2$I$_2$]$^{2-}$), self-trapped exciton (STE) emissions dominate, completely suppressing organic afterglow. Furthermore, (BuTPP)$_2$ZnCl$_4$ glass exhibits excitation-dependent multicolor phosphorescence due to aggregate cluster luminescence. These glasses showcase dual-mode emissions (RTP/STE) and are successfully applied in shape-controllable anti-counterfeiting and high-resolution X-ray scintillation imaging (10 lp mm^{-1}). This work provides a facile vitrification strategy and design principles for hybrid RTP materials with tailored photophysical properties.

1 Introduction

Room temperature phosphorescence (RTP) is a fascinating optical phenomenon characterized by long-lived emission that can persist from several microseconds to even seconds under ambient conditions after the cessation of excitation.[1–4] Owing to its distinct photophysical features, such as extended luminescence decay lifetime and large Stokes shift, it has garnered significant attention for a wide range of applications, including anti-counterfeiting, bioimaging, and light-emitting devices.[5–8] Over the last few years, pure organic phosphors have been extensively studied due to their tunable molecular structures, easy modification and processing, excellent biocompatibility, and high mechanical flexibility.[1,3,9–11] Nevertheless, the intrinsic weak spin–orbit coupling (SOC) effect and low radiative recombination rate of organic phosphors lead to low phosphorescence efficiency, which limits their practical applications.

Recently, zero-dimensional (0D) organic–inorganic hybrid metal halides have emerged as promising candidates for RTP materials by integrating the advantages of both organic and inorganic constituents.[12–19] In particular, the intrinsic RTP characteristics arising from triplet excitons of organic cations contribute significantly to the diversification of luminescent properties of hybrid metal halides. Meanwhile, the optically inert metal halide units provide a rigid structural framework and introduce the heavy-atom effect, which effectively enhances the afterglow emission of the organic components in these hybrid metal halides.[12,13] Benefiting from these combined optical and structural merits, 0D organic–inorganic hybrid metal halides are considered to be one of the most desirable RTP materials. For example, Ma *et al.* reported a series of 0D TPP$_2$ZnX$_4$ (X = Cl, Br) exhibiting efficient RTP with tunable lifetimes ranging from 215.5 to 37.2 ms.[13] Similarly, Yan and co-workers developed a 0D (Ph$_4$P)$_2$Cd$_2$Br$_6$, which demonstrates excellent luminescent stability over a broad temperature range (100–320 K), along with a high RTP quantum yield of 62.79% and a lifetime of 37.85 ms.[15] To date, hybrid metal halide RTP materials have predominantly existed in the form of single crystals and powders.[12,13] However, these forms suffer from poor processability, and face challenges in constructing large-scale, shape-controllable devices required for practical applications.

Hybrid metal halide glasses, are an emerging class of luminescent materials, offer distinct advantages over their crystalline counterparts.[14,20–22] Notably, they feature high transparency, excellent processability, high mechanical rigidity and durability, making them highly attractive in photonic fields.[20,21] In addition, the closely packed three-dimensional (3D) networks in these hybrid glasses provide a rigid and confined

Key Laboratory of Materials Physics of Ministry of Education, School of Physics, Zhengzhou University, Zhengzhou 450052, China. E-mail: shizf@zzu.edu.cn

microenvironment that effectively suppresses non-radiative relaxation of triplet excitons, thereby promoting RTP.[21,23–25] Moreover, hybrid glasses can serve as prospective host matrices with high structural tolerance, enabling the incorporation of various metal halide structural units.[20,22,26–28] For example, the emissive metal halide structure units, such as $[MnBr_4]^{2-}$ tetrahedrons and $[SbCl_5]^{2-}$ pyramids, have been successfully incorporated into the hybrid glasses, exhibiting bright green and orange emissions, respectively.[20,22,26,29] However, as long as the emissive metal halide units are present in 0D hybrid glasses, the energy transfer from organic triplet states to inorganic emission centers with shorter lifetimes will occur, as a result, the afterglow emission of organic components is suppressed in these glasses. Therefore, introducing the optically inert metal halide units to them is beneficial to realize the RTP in 0D hybrid metal halide glasses. Furthermore, these hybrid glasses provide an excellent platform for tuning the intrinsic RTP properties of organic cations by leveraging the heavy-atom effect of inert inorganic metal halide units.[13] However, the on-demand manipulation of RTP properties to achieve desirable phosphorescent performance remains a formidable challenge. Therefore, in depth studies on how inorganic heavy-atom units influence the RTP properties of organic components are essential for the rational design of advanced RTP materials.

However, the fabrication of glassy hybrid metal halides remains challenging due to their relatively weak glass-forming ability.[30–32] This limitation primarily arises from the premature dissociation of organic components before the melting of precursors using the mainstream melt-quenching method, as well as a strong propensity for recrystallization during the quenching process.[32] Consequently, the development of alternative vitrification strategies, particularly those that circumvent the melting process, is of great significance for advancing multifunctional hybrid metal halide glasses.

In this work, we present a facile solvent-assisted rapid evaporation method to synthesis a series of 0D butyltriphenylphosphonium-based (BuTPP$^+$) hybrid metal halide glasses with a well-defined composition of (BuTPP)$_2$-MCl$_2$X$_2$. The BuTPP$^+$ is selected as the organic cation, due to its characteristic long-lived phosphorescence emission, a series of optically inert, heavy-atom-containing metal halide anions $[MCl_2X_2]^{2-}$ (such as $[ZnCl_4]^{2-}$, $[CdCl_4]^{2-}$, $[ZnCl_2Br_2]^{2-}$, $[CdCl_2Br_2]^{2-}$, $[ZnCl_2I_2]^{2-}$, and $[CdCl_2I_2]^{2-}$), are introduced to tune the RTP properties of (BuTPP)$_2$MCl$_2$X$_2$ glasses. Significantly, as the atomic number of inorganic metal halide units increases, the phosphorescence decay lifetime of the triplet state of BuTPP$^+$ gradually decreases due to the heavy-atom effect. More importantly, when the atomic number of inorganic metal halide unit exceeds 170, (BuTPP)$_2$MCl$_2$X$_2$ glasses (as in the cases of $[ZnCl_2I_2]^{2-}$, and $[CdCl_2I_2]^{2-}$) exhibit the self-trapped exciton (STE) emissions with faster decay lifetimes, while the afterglow emission of BuTPP$^+$ is completely suppressed. Interestingly, aggregate cluster luminescence is observed in (BuTPP)$_2$ZnCl$_4$ glass, exhibiting excitation-dependent multicolor phosphorescence. These novel 0D hybrid metal halide glasses, featuring both long-lived RTP and short-lived STE emissions, are demonstrated in applications such as shape-controllable anti-

counterfeiting and X-ray scintillation imaging. Fig. 1d summarized the key features of this study. This work not only provides an effective strategy for synthesizing hybrid metal halide glasses but also offers valuable insights for designing hybrid RTP materials with tunable photophysical properties.

2 Results and discussion

In this work, we present a solvent-assisted rapid evaporation method that bypasses the conventional melting process for the fabrication of glass materials. As a representative system, (BuTPP)$_2$ZnCl$_4$ was selected to investigate the glass formation behavior (Fig. 1a). In a typical synthesis, BuTPPCl and ZnCl$_2$ precursors at a 2 : 1 molar ratio were dissolved in a mixed solvent of dimethyl sulfoxide (DMSO) and deionized water, yielding a homogeneous and transparent precursor solution. This solution was then transferred to a glass dish and heated to 200 °C, triggering rapid solvent evaporation. The glass formation process proceeds through the following three distinct stages: (1) solution concentration: initially, at 200 °C, rapid solvent evaporation reduces the solvent content, drawing the building blocks into closer proximity and facilitating non-covalent interactions such as hydrogen bonding and ionic interactions. (2) Viscoelastic transition: continued evaporation increases the solution's viscosity, transitioning it into a viscoelastic glassy liquid analogous to a supercooled liquid in the melt-quenching process (Fig. S1a).[33] This elevated viscosity kinetically inhibits crystallization by limiting molecular mobility. (3) Vitrification: ongoing solvent removal ultimately yields a homogeneous, transparent glass with a diameter of 6 cm (Fig. 1b). This strategy enables the rapid and straightforward synthesis of a series of hybrid metal halide glasses with high transparency and tunable RTP properties by incorporating various optically inert metal halide units (Fig. 1c). Control experiments reveal that slower evaporation at room temperature leads to crystallization of (BuTPP)$_2$ZnCl$_4$ (Fig. 1a), underscoring the critical role of evaporation rate in achieving vitrification.

The synthesis route followed the same procedure as that for the (BuTPP)$_2$ZnCl$_4$ glass, except that ZnCl$_2$ was excluded. In this case, glass formation was not achieved, and the material crystallized instead (Fig. S1b), indicating that the A-site organic molecules alone cannot form a glassy phase. Additionally, we attempted to directly prepare the glass by uniformly mixing BuTPPCl and ZnCl$_2$, followed by heating the mixture to 200 °C. However, as shown in Fig. S1c, the mixture did not fully melt under these conditions, and no transparent glass was obtained after cooling to room temperature, indicating that the conventional direct melt-quenching method is insufficient to achieve vitrification in this system. The glass-forming ability of P-ZnCl$_2$ can be attributed to three main factors: (1) Hydrogen bonding interactions: strong multiple hydrogen bonds among DMSO, H$_2$O, BuTPP$^+$, and $[ZnCl_4]^{2-}$ stabilize the disordered network. Rapid solvent evaporation prevents molecular rearrangement, favoring glass formation.[33] (2) Bulky organic cations: the glass-forming ability is strongly correlated with crystallization resistance. Incorporating large organic cations with high steric
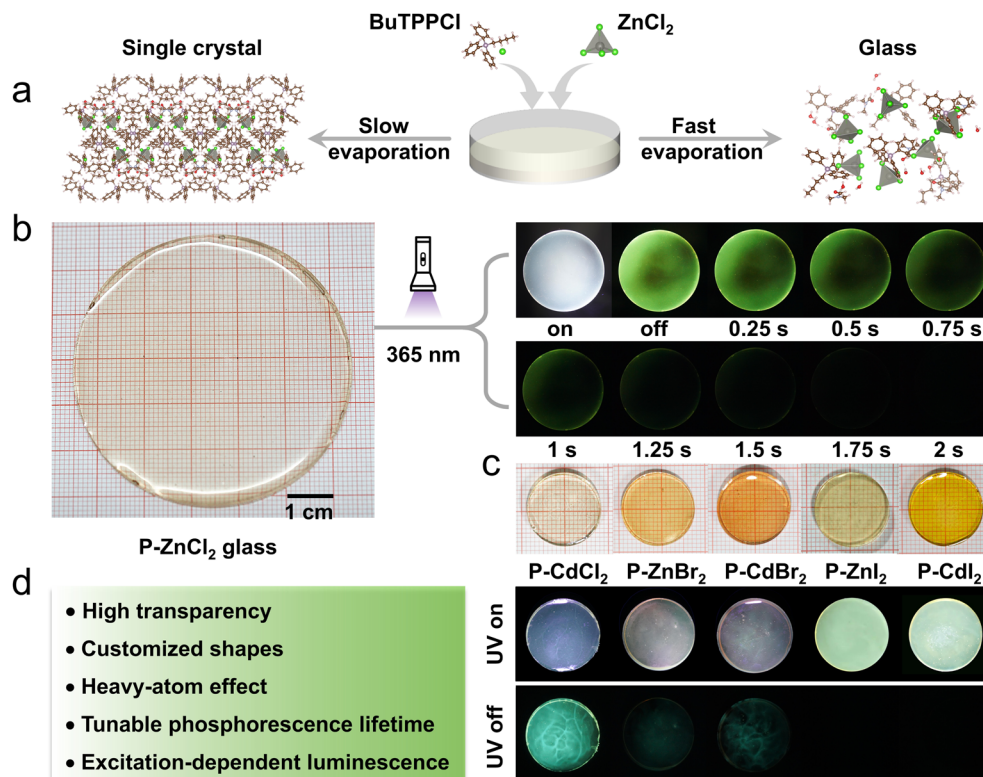
Fig. 1 (a) Schematic diagram of illustrating the controllable synthesis of P-ZnCl$_2$ glass and crystal *via* the solvent-assisted rapid and slow evaporation method. The left side shows the crystal structure of P-ZnCl$_2$ single crystal, and the right side shows the amorphous molecular structure of P-ZnCl$_2$ glass. (b) Photographs of P-ZnCl$_2$ glass with a diameter of 6 cm under ambient light, UV irradiation (365 nm), and UV off. (c) Photographs of P-CdCl$_2$, P-ZnBr$_2$, P-CdBr$_2$, P-ZnI$_2$, and P-CdI$_2$ glasses under ambient light, UV irradiation (365 nm), and UV off. (d) The typical features of the (BuTPP)$_2$MCl$_2$X$_2$ glasses.

hindrance effectively suppresses crystallization.[22] Previous studies have shown that small cations promote nucleation and crystallization during quenching, whereas bulky cations favor glass formation.[26] In this work, bulky organic cations BuTPP$^+$, containing three benzene rings and one branched group, provides significant steric hindrance that inhibits crystallization. (3) High viscosity: the high viscosity of the glass liquid further restricts the movement of organic and inorganic species, preventing crystallization during quenching. These three factors collectively enable the successful formation of the P-ZnCl$_2$ glass.

Fig. 1b and c show images of the as-prepared (BuTPP)$_2$ZnCl$_4$ (abbreviated as P-ZnCl$_2$), (BuTPP)$_2$CdCl$_4$ (P-CdCl$_2$), (BuTPP)$_2$-ZnCl$_2$Br$_2$ (P-ZnBr$_2$), (BuTPP)$_2$CdCl$_2$Br$_2$ (P-CdBr$_2$), (BuTPP)$_2$-ZnCl$_2$I$_2$ (P-ZnI$_2$), and (BuTPP)$_2$CdCl$_2$I$_2$ (P-CdI$_2$) glasses under ambient light, ultraviolet (UV) irradiation (365 nm), and UV off. Upon UV irradiation, P-ZnCl$_2$, P-CdCl$_2$, P-ZnBr$_2$, and P-CdBr$_2$ exhibit bright white-light emission, whereas P-ZnI$_2$ and P-CdI$_2$show cyan emission. Notably, once the UV lamp is turned off, the emissions disappeared immediately for P-ZnI$_2$ and P-CdI$_2$ glasses, while the green afterglow emissions from P-ZnCl$_2$, P-CdCl$_2$, P-ZnBr$_2$, and P-CdBr$_2$ were observed with naked eyes. These observations highlight the critical influence of the heavy-atom effect from the inorganic metal halide units on the emission characteristics, particularly in modulating RTP

behavior in hybrid metal halide glasses. The crystal structure of P-ZnCl$_2$ single crystals was determined by single-crystal X-ray diffraction (SCXRD). As shown in Fig. 1a, P-ZnCl$_2$ crystal crystallizes in the orthorhombic space group $Pca2_1$, in which the [ZnCl$_4$]$^{2-}$ tetrahedrons are completely isolated from each other and periodically embedded in the matrix of large organic cations BuTPP$^+$, forming a 0D crystal structure at the molecular level. The Zn^{2+} ion adopts a typical tetrahedral coordination geometry, bonded to four Cl atoms with an average Zn–Cl bond length of 2.28 Å and an average Cl–Zn–Cl bond angle of 109.47°, consistent with previously reported [ZnCl$_4$]$^{2-}$ tetrahedrons in other Zn-based metal halides.[16,17] More detailed crystal diffraction data are summarized in Table S1.

The formation of P-ZnCl$_2$ glass was confirmed by powder X-ray diffraction (PXRD). As shown in Fig. 2a, in contrast to the crystal counterpart that displays sharp characteristic diffraction peaks, the as-prepared P-ZnCl$_2$ glass exhibits a broad diffuse diffraction band, indicating the highly disordered amorphous structure.[20] To further investigate the organic molecular structure within the P-ZnCl$_2$ glass, Fourier transform infrared (FTIR) and proton nuclear magnetic resonance (^{1}H NMR) spectroscopy were conducted. The FTIR spectra of the P-ZnCl$_2$ glass and crystal samples are nearly identical (Fig. 2b), suggesting that the chemical structure of the organic cations BuTPP$^+$ remains intact after vitrification. Specifically, the absorption bands between
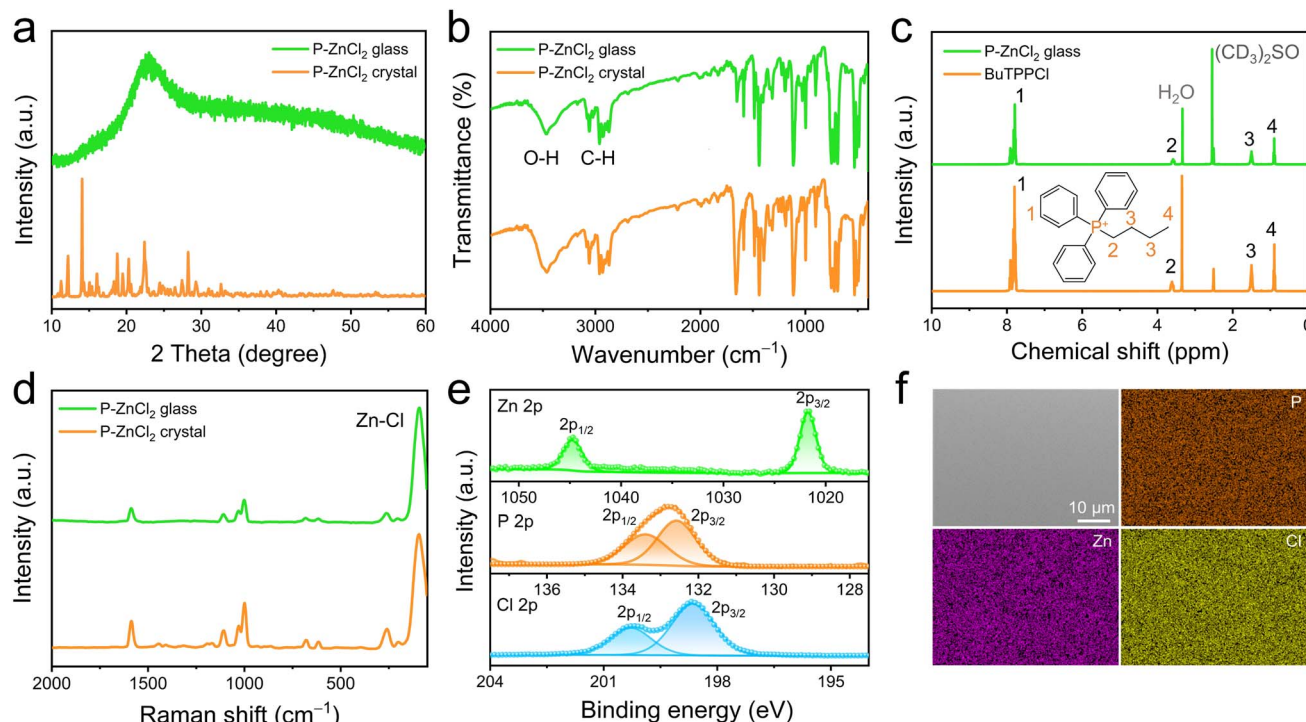
Fig. 2 (a) PXRD patterns of P-ZnCl$_2$ glass and crystal. (b) FTIR spectra of P-ZnCl$_2$ glass and crystal. (c) ^{1}H NMR spectra of P-ZnCl$_2$ glass and BuTPPCl molecule. (d) Raman spectra of P-ZnCl$_2$ glass and crystal. (e) High-resolution XPS spectra of Zn 2p, P 2p, and Cl 2p in P-ZnCl$_2$ glass. (f) SEM image and EDS elemental mapping of P, Zn, and Cl in P-ZnCl$_2$ glass.

400 and 1600 cm^{-1} are assigned to the C–H stretching vibrations of phenyl rings, while the peaks near 3000 cm^{-1} correspond to the sp^3-hybridized C–H bonds in butyl chains.[34] Additionally, a broad band centered at 3470 cm^{-1} is attributed to the O–H group vibrations, indicating the presence of hydrogen bonding interactions within the glass matrix.[2] The ^{1}H NMR spectrum further confirms the structural integrity of organic cations BuTPP$^+$ in P-ZnCl$_2$ glass, as shown in Fig. 2c. After excluding the signals from the solvent ((CD$_3$)$_2$SO) and water (H$_2$O), the spectrum of P-ZnCl$_2$ glass exhibits four distinct proton environments. These are attributed to aromatic protons (δ1 = 7.5–8.1 ppm), and adjacent to the triphenylphosphonium core protons (δ2 = 3.4–3.7), interstitial protons (δ3 = 1.3–1.7), and terminal protons (δ4 = 0.7–1.0) of the butyl chain, with integration areas of 15.00, 2.00, 4.00, and 3.00, respectively. The integration ratio of 15 : 2 : 4 : 3 is consistent with the theoretical proton counts, confirming that the structure of organic cations BuTPP$^+$ is preserved during glass formation.[35]

Raman spectroscopy was employed to investigate the chemical bonding characteristics in P-ZnCl$_2$ glass. As shown in Fig. 2d, the nearly identical peak patterns in the Raman spectra for both the glass and crystal phases further confirm the similarity in the chemical environment of their inorganic [ZnCl$_4$]$^{2-}$ tetrahedrons. Clearly, the Raman spectrum of the P-ZnCl$_2$ glass retains the characteristic vibrational features associated with both the inorganic [ZnCl$_4$]$^{2-}$ tetrahedrons and the carbon backbone structure of organic cations BuTPP$^+$ (Fig. 2d). In detail, the Raman shift in the 50–300 cm^{-1} range corresponds

to the Zn–Cl bond stretching vibrations from the [ZnCl$_4$]$^{2-}$ tetrahedrons,[36] while the 500–1700 cm^{-1} range is assigned to the alkyl C–C bonds vibrations from the organic cations BuTPP$^+$, including a prominent benzene ring vibration mode at 1000 cm^{-1}.[34] Moreover, to confirm the chemical composition and valence states of the elements in P-ZnCl$_2$ glass, X-ray photoelectron spectroscopy (XPS) measurements were carried out and revealed the existence of P, Zn, and Cl elements in the P-ZnCl$_2$ glass. As shown in Fig. 2e, the high-resolution Zn 2p spectrum displays double characteristic peaks at 1044.8 eV (2p$_{1/2}$) and 1021.7 eV (2p$_{3/2}$) with an energy separation of 23.1 eV, demonstrating the divalent state of Zn in the P-ZnCl$_2$ glass.[16] In addition, the corresponding binding energies of P 2p and Cl 2p spectra are consistent with the characters of P$^+$ and Cl$^-$ in the P-ZnCl$_2$ glass.[37,38] These complementary spectroscopic analyses provide conclusive evidence for the successful formation of P-ZnCl$_2$ glass, clearly demonstrating that both the structural integrity of the organic cation BuTPP$^+$ and the characteristic tetrahedral coordination geometry of the inorganic [ZnCl$_4$]$^{2-}$ anions are well-preserved in the resulting amorphous phase.

The micromorphology and elemental distribution of the as-prepared P-ZnCl$_2$ glass were further characterized using scanning electron microscopy (SEM) and energy-dispersive X-ray spectroscopy (EDS). As shown in Fig. 2f, the SEM image reveals a compact and smooth surface, indicating a high-quality amorphous phase. EDS elemental mapping confirms the homogeneous distribution of P, Zn, and Cl throughout the P-ZnCl$_2$ glass. Moreover, the quantitative EDS elemental analysis

yields an average atomic ratio of P : Zn : Cl = 27.87 : 56.56 : 15.57 (Fig. S2), which is consistent with the stoichiometric ratio of P-ZnCl$_2$. This characteristic surface structure effectively minimizes light scattering caused by surface pores or crystal boundaries, thereby contributing to the high optical transparency of the glass.[20] The thermal behavior of P-ZnCl$_2$ glass was evaluated using thermogravimetric analysis (TGA) and differential scanning calorimetry (DSC). As shown in the TGA curve (Fig. S3), the P-ZnCl$_2$ glass exhibits a high decomposition temperature (T_d) of 280 °C, demonstrating its excellent thermal stability. The glass transition temperature T_g is the characteristic temperature at which an amorphous material transitions from a hard and brittle glassy state to a soft and rubbery or viscous supercooled liquid state upon heating. The DSC curve reveals a clear glass transition temperature (T_g) at 49.5 °C (Fig. S4), further confirming the successful vitrification of the material and its amorphous nature.[27] From a practical perspective, it is worth noting that further enhancement of the T_g in hybrid metal halide glasses represents an essential direction for future research to improve their thermal stability and broaden their potential applications. As shown in Fig. S5, the ultraviolet-visible (UV-vis) absorption spectra of these hybrid metal halide glasses exhibit strong absorption in the range of 200–400 nm, consistent with their appearance under natural light. The high energy absorption peaks at around 276 nm can be attributed to the π–π* transitions of the phenyl moieties in the BuTPP$^+$ cations.[12] The observed low energy absorption bands spanning 300–410 nm can be attributed to the intermolecular charge transfer state, with these UV-vis absorption characteristics demonstrating the coexistence of multiple distinct electronic transition processes.[12] Moreover, these hybrid metal halide glasses display only a broad peak (Fig. S6), confirming their fully amorphous structure, which arises from random molecular arrangements within the glass matrix.[14]

The resulting six hybrid metal halide glasses exhibit high optical transparency, as shown in Fig. 3a, with over 80% transmittance in the range of 400–800 nm. To investigate how the metal halide species influence RTP behavior, the photophysical properties of these glasses were systematically studied. The prompt and delayed (acquired after 5 ms of excitation) PL spectra were recorded under 300 nm excitation (Fig. 3b). As shown in Fig. S7, the organic molecule BuTPPCl exhibits dual-band emission characteristics, featuring a fluorescence peak at 337 nm with a short lifetime of 1.87 ns, and a phosphorescence peak at 492 nm with a longer lifetime of 1032 ms.[13] Upon incorporating BuTPP$^+$ with optically inert metal halide units (such as [ZnCl$_4$]$^{2-}$, [CdCl$_4$]$^{2-}$, [ZnCl$_2$Br$_2$]$^{2-}$, and [CdCl$_2$Br$_2$]$^{2-}$), the resulting four hybrid metal halide glasses display prompt PL spectra similar to that of organic molecule BuTPPCl, with only slight variations in fluorescence and phosphorescence intensities and peak positions (Fig. 3b). The delayed PL spectra of these hybrid glasses also show the same phosphorescence profiles as BuTPPCl, indicating that the afterglow emissions originate primarily from the organic cations BuTPP$^+$. Time-resolved PL decay curves show that the emission lifetimes of the four hybrid glasses, monitored at 492 nm, decrease significantly with the incorporation of heavier metal halide species (Fig. 3c). Specifically, as shown in Fig. 3d, the PL decay lifetimes decrease from 608.6 ms for P-ZnCl$_2$ to 550.3 ms for P-CdCl$_2$, 179.8 ms for P-ZnBr$_2$, and 146 ms for P-CdBr$_2$. This reduction in phosphorescence lifetime is attributed to the heavy-atom effect: the inclusion of heavier metal halide units enhances spin–orbit coupling, which in turn facilitates intersystem crossing (ISC) rate k_{ISC} from 5.69×10^7 s^{-1} to 8.32×10^7 s^{-1} (Table S2).[13] As a result, the radiative decay rate k_p from the triplet state is accelerated (Table S2), leading to shorter phosphorescence lifetimes.[39] The fluorescence lifetimes of these hybrid metal halide glasses are shown in Fig. S8. The luminescence kinetic parameters of these hybrid glasses are summarized in Table S2.

Further density functional theory (DFT) calculation was performed to rationally predict the energy gaps among the ground state (S$_0$), singlet (S$_1$) and triplet (T$_1$) states, which can be used to evaluate the heavy-atom effect and ISC rate. According to the perturbation theory, the ISC rate is inversely proportional to the energy gap between singlet and triplet excited state, that is, small energy gap is in favor of ISC rate. Based on the calculated excited structures (Fig. S9), the energy gap between S$_1$ and T$_1$ of P-ZnBr$_2$ (0.164 eV) is smaller than that of P-ZnCl$_2$ (0.566 eV), indicating that the reduced gap in P-ZnBr$_2$ facilitates ISC and enhances phosphorescence generation. Similarly, the energy gap between S$_1$ and T$_1$ of P-CdBr$_2$ (0.321 eV) is smaller than that of P-CdCl$_2$ (0.632 eV). Moreover, the calculated SOC coefficients between S$_1$ and T$_1$ in (BuTPP)$_2$-MCl$_2$X$_2$ increase with the atomic number of the inorganic metal halide units, suggesting that heavier inorganic metal halide units induce stronger SOC interactions and thus higher ISC rates. These theoretical results clearly demonstrate that the incorporation of inorganic metal halide units introduces a pronounced heavy-atom effect, promoting ISC and enabling efficient phosphorescence generation in (BuTPP)$_2$MCl$_2$X$_2$ glasses, which is consistent with the experimental observations. The pronounced heavy-atom effect from the inorganic metal halide species provides a reliable approach for predicting and tuning the phosphorescence lifetimes. The modulation of inorganic metal halide species in 0D hybrid metal halide glasses is an effective strategy to design RTP materials with anticipated phosphorescence lifetimes. Based on this strategy, we deliberately selected [SrCl$_4$]$^{2-}$ with an atomic number of 106 as an intermediate between [ZnCl$_4$]$^{2-}$ and [CdCl$_4$]$^{2-}$ to construct (BuTPP)$_2$SrCl$_4$ (P-SrCl$_2$) glass, anticipating an intermediate phosphorescence lifetime. Remarkably, the prepared P-SrCl$_2$ glass not only retained the characteristic dual-band emission of BuTPPCl but also exhibited a phosphorescence lifetime of 592 ms (Fig. S10), perfectly matching our predicted lifetime range (Fig. 3d), thereby validating our design principle.

Distinct from the triplet phosphorescence spectrum characterized by three sublevels, the broad Gaussian-shaped prompt PL emission, large Stokes shift, and microsecond lifetimes observed in P-ZnI$_2$ and P-CdI$_2$ glasses (Fig. 3b and c), which are characteristic features of STE emission.[40–42] The identical wavelength-dependent PLE and PL spectra further confirm that these PL emissions originate from the relaxation of the same excited state (Fig. S11 and S12).[43] Additionally, the PL intensities
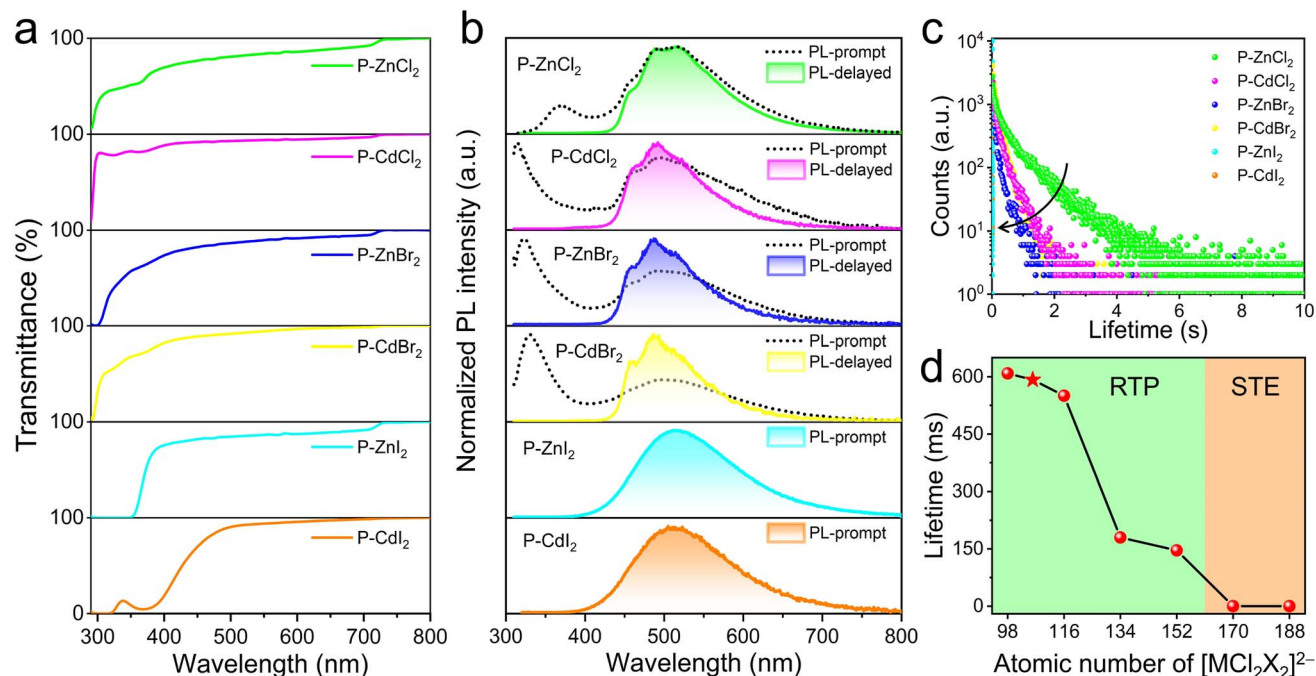
Fig. 3 (a) Transmittance spectra of (BuTPP)$_2$MCl$_2$X$_2$ glasses. (b) The prompt and delayed PL spectra of (BuTPP)$_2$MCl$_2$X$_2$ glasses. (c) Time-resolved phosphorescence decay curves of (BuTPP)$_2$MCl$_2$X$_2$ glasses. (d) The phosphorescence lifetimes of (BuTPP)$_2$MCl$_2$X$_2$ glasses as a function of atomic number of [MCl$_2$X$_2$]$^{2-}$ in (BuTPP)$_2$MCl$_2$X$_2$ glasses.

of P-ZnI$_2$ and P-CdI$_2$ glasses gradually increase with decreasing temperature (Fig. S13a and S14a). Meanwhile, the thermal activation energy (E_a) is considered to evaluate the exciton binding energy, which can be estimated by Arrhenius equation.[38] The E_a values for P-ZnI$_2$ and P-CdI$_2$ were calculated to be 67.18 and 66.16 meV (Fig. S13b and S14b), respectively. The high values of E_a in both samples indicate the formation of stable STEs. Due to the strong and fast nature of STE emission, it dominates the prompt PL spectra (Fig. 3b).

Based on the above results, the possible energy transfer pathways are illustrated in Fig. 4. The excited state energy levels and emission energy levels are calculated based on the excitation and emission wavelengths of these materials (Fig. S15). As for organic molecule BuTPPCl, photoexcitation promotes electrons to the singlet state S$_1$, from which some electrons relax to

the ground state S$_0$, producing fluorescence. Others undergo an ISC process to the triplet states (T$_1$, T$_2$, T$_3$), resulting in afterglow emission. For P-ZnCl$_2$, P-CdCl$_2$, P-ZnBr$_2$, and P-CdBr$_2$, the observed triplet phosphorescence originates not only from the singlet state of organic cation BuTPP$^+$, but also from the energy transfer involving the inorganic metal halide units. As shown in Fig. S7a, the delayed PL spectra of BuTPPCl molecule reveal three triplet sublevels (T$_1$, T$_2$, and T$_3$), with the T$_2$ emission located at 492 nm. The excitation spectrum monitored at 492 nm matches that of the singlet state (Fig. S7b), indicating that the triplet emission in BuTPPCl primarily arises from the singlet state. Upon incorporation of ZnCl$_2$, the resulting P-ZnCl$_2$ glass exhibits a similar triplet phosphorescence profile to that of BuTPPCl (Fig. 3b). However, the excitation spectrum monitored at 492 nm for the triplet emission not only overlaps with the
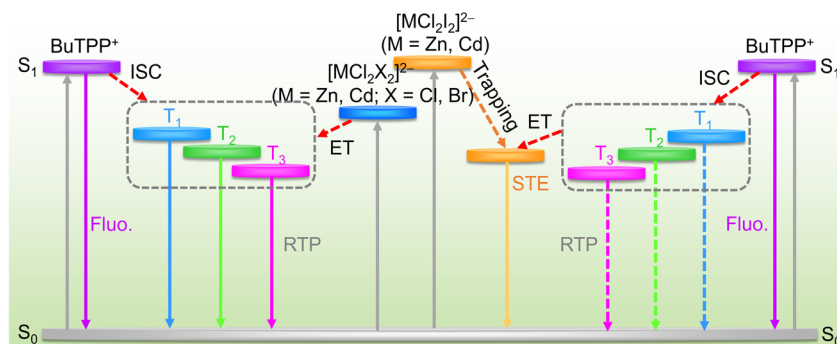

Fig. 4 Schematic illustrations of the excited states alignments, energy transfer and relaxation paths of excited states in (BuTPP)$_2$MCl$_2$X$_2$ glasses.

singlet state excitation spectrum but also displays an additional low-energy broadband excitation peak at 426 nm (Fig. S15a), suggesting that the triplet luminescence originates from both the singlet state and newly introduced inorganic metal halide units (Fig. 4). For P-CdCl$_2$, P-ZnBr$_2$, and P-CdBr$_2$, the photoluminescence excitation (PLE) spectra also exhibit the same characteristics, that is the PLE spectrum not only overlaps with the singlet state excitation spectrum, but also exhibits a new low-energy broadband excitation peak (Fig. S15b–d), indicating that the triplet luminescence not only originates from the singlet state, but also from newly introduced inorganic metal halide units [MCl$_2$X$_2$]$^{2-}$ (Fig. 4). The harvested excitons from [MCl$_2$X$_2$]$^{2-}$ can efficiently populate the triplet states of BuTPP$^+$, thereby enhancing its phosphorescence. Substitution of Cl with Br and Zn with Cd in [ZnCl$_2$X$_2$]$^{2-}$ introduces heavy-atom effect and enhances SOC, accelerating ISC and reducing the phosphorescence lifetimes. Consequently, P-CdBr$_2$ exhibits the shortest afterglow lifetime among the four (BuTPP)$_2$MCl$_2$X$_2$ glasses.

In the case of P-ZnI$_2$ and P-CdI$_2$ glasses, the PL spectra exhibit Gaussian-shaped emission profiles, which differs from the triplet phosphorescence spectrum of BuTPPCl containing three sublevels (Fig. 3b). The time-resolved PL decay spectrum of P-ZnI$_2$ (P-CdI$_2$) glass monitored at 492 nm emission shows a lifetime of 2.18 (2.13) μs (Fig. S16a and b), characteristic of STE state. To investigate whether long-lived triplet luminescence exists in P-ZnI$_2$ (P-CdI$_2$) glass, we tested the time-resolved PL decay spectrum at 492 nm with a 1 ms delay to eliminate the contribution from STE emission. As shown in Fig. S16c and d, after a delay of 1 ms, almost no photon signal was detected, indicating the absence of triplet state luminescence. This suggests efficient energy transfer from the triplet excitons of BuTPP$^+$ to the STE states of the inorganic metal halide units, resulting in detectable emission solely from STE excitons. Furthermore, temperature-dependent time-resolved PL decay curves of P-ZnI$_2$ glass monitored at 492 and 516 nm emission were measured. As shown in Fig. S17, as the temperature increases from 80 to 300 K, the decay lifetime remains in the microsecond range, confirming that STE dominates the emission even at low temperatures. Theoretically, the energy transfer efficiency (η_{ET}) from BuTPP$^+$ to STE state is calculated by following equation,

$$\eta_{ET} = 1 - \frac{\tau_{STE}}{\tau_T}$$

where τ_T represents the triplet exciton lifetime of the donor monitored at 492 nm in BuTPPCl, while τ_{STE} denotes the luminescence lifetime of the donor in the presence of the STE acceptor in P-ZnI$_2$ and P-CdI$_2$ glasses. Significantly, both the energy transfer efficiency were calculated to be near-unity for P-ZnI$_2$ and P-CdI$_2$ glasses.

Interestingly, the experimental results revealed that P-ZnCl$_2$ glass exhibits excitation wavelength-dependent multicolor luminescence. This phenomenon was quantitatively recorded by the two-dimensional (2D) excitation–emission matrix spectra (Fig. 5a). For instance, under 350 nm excitation, P-ZnCl$_2$ glass shows a maximum emission peak at 518 nm, whereas shifting

the excitation to 600 nm results in a redshifted emission peak at 659 nm (Fig. S18). The color variations of the P-ZnCl$_2$ glass under different excitation wavelengths were illustrated in the Commission Internationale de l'Eclairage (CIE) chromaticity coordinate diagram (Fig. 5b), showing a continuous shift in emission color from blue to white to red as the excitation wavelength increased from 250 to 650 nm. To the best of our knowledge, such a broad range of excitation-dependent colorful luminescence is rarely reported in hybrid metal halides. This excitation-dependent emission could be attributed to the presence of multiple luminescent centers within the glass matrix.[41,44] Time-resolved PL decay measurements further revealed that the excited state lifetimes of P-ZnCl$_2$ glass was dependent on the excitation wavelength, exhibiting tunable phosphorescence lifetimes ranging from 0.11 to 15.34 ms as the excitation wavelength shifts from 350 to 600 nm (Fig. 5c). These distinct variations in excited state lifetimes further confirmed the existence of disparate emissive species.[4,8,45,46] In contrast, no excitation-dependent emission behavior is observed in BuTPPCl molecule (Fig. 5d), indicating its isolated luminescent feature.[2] Moreover, the excitation spectra of P-ZnCl$_2$ glass exhibit a progressive redshift with increasing emission wavelength (Fig. 5e), suggesting that the excitation-dependent multicolor phosphorescence arises from multiple aggregate clusters in P-ZnCl$_2$ glass.[33,46,47] These diverse aggregates likely form cascade excited states that give rise to the observed multicolor emissions (Fig. 5f).

The PL spectra of P-ZnCl$_2$ glass under the variable excitation light power were measured. As shown in Fig. S19, the PL intensity of P-ZnCl$_2$ glass exhibited a linear dependence on excitation power, ruling out the possibility of defect state luminescence. The delayed PL spectra of P-ZnCl$_2$ glass with delay times ranging from 1 to 80 ms were recorded, as shown in Fig. S20. As the delay time increases, the intensity of different luminescent centers gradually decreases, indicating the existence of different luminescent species. Additionally, to further investigate the cluster structure of P-ZnCl$_2$ glass, 2D grazing-incidence wide-angle X-ray scattering (GiWAXS) patterns and one-dimensional (1D) scattering profiles along the q_z direction were conducted. P-ZnCl$_2$ glass exhibits an intensified central scattering signal (Fig. S21a), suggesting strong molecular aggregation. Distinct scattering peaks appear at $q = 0.74$, 0.95, 1.42, 1.67 Å^{-1} (Fig. S21b), corresponding to π–π stacking distances of 8.49, 6.61, 4.42, 3.76 Å, respectively, as calculated using Bragg's equation $d = 2\pi/q$.[47] These peaks originate from multiple aggregated clusters within the glass matrix. At q values above 1.75 Å^{-1}, the scattering intensity rapidly decays, indicating the absence of long-range structural periodicity at the molecular level. This observation is consistent with the amorphous structural characteristics of P-ZnCl$_2$ glass. The 2D excitation–emission matrix spectra of the other three glasses, P-CdCl$_2$, P-ZnBr$_2$, and P-CdBr$_2$, were also recorded. All of them exhibit excitation-dependent multicolor luminescence (Fig. S22), similar to that observed for the P-ZnCl$_2$ glass.

Benefiting from the moldability of glasses and time-resolved RTP properties of these hybrid metal halide glasses, these materials exhibit great potential for multifunctional anti-
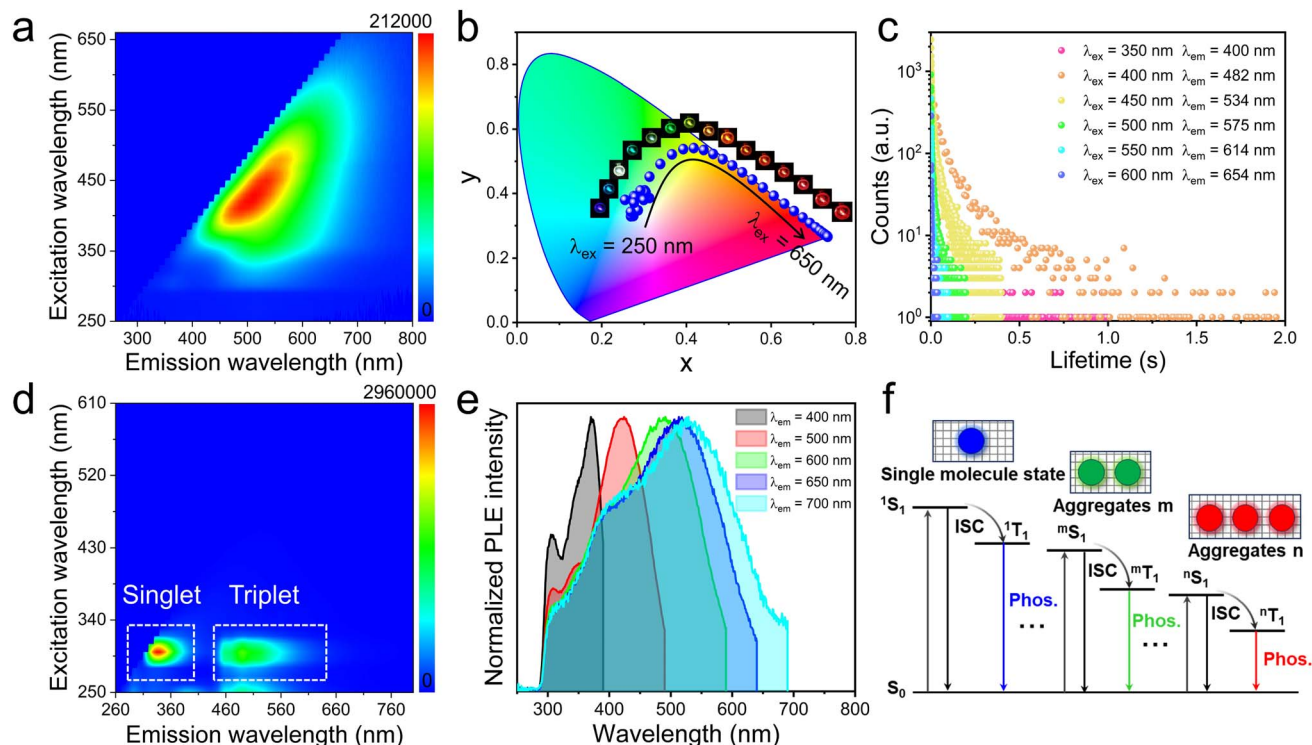
Fig. 5 (a) 2D excitation–emission matrix spectra of P-ZnCl$_2$ glass at room temperature. (b) CIE chromaticity coordinate diagram of P-ZnCl$_2$ glass at various excitation wavelengths. Insets show luminescence photographs of P-ZnCl$_2$ glass under various excitation wavelengths. (c) Time-resolved PL decay curves of P-ZnCl$_2$ glass under different excitation and emission wavelengths. (d) 2D excitation–emission matrix spectra of BuTPPCl molecule at room temperature. (e) Excitation spectra of P-ZnCl$_2$ glass monitored at different emission wavelengths at room temperature. (f) Proposed mechanism of multicolor luminescence at different excitation wavelengths with multiple aggregate clusters in P-ZnCl$_2$ glass.

counterfeiting applications. As illustrated in Fig. 6a, a series of hybrid metal halide glasses were shaped into distinct letters, including "R" from P-ZnCl$_2$, "T" from P-CdCl$_2$, and "P" from P-ZnBr$_2$. Under 365 nm UV lamp irradiation, these patterns emit bright white-light emissions. Once the UV light is turned off, the letters "R" and "T" immediately display green afterglow
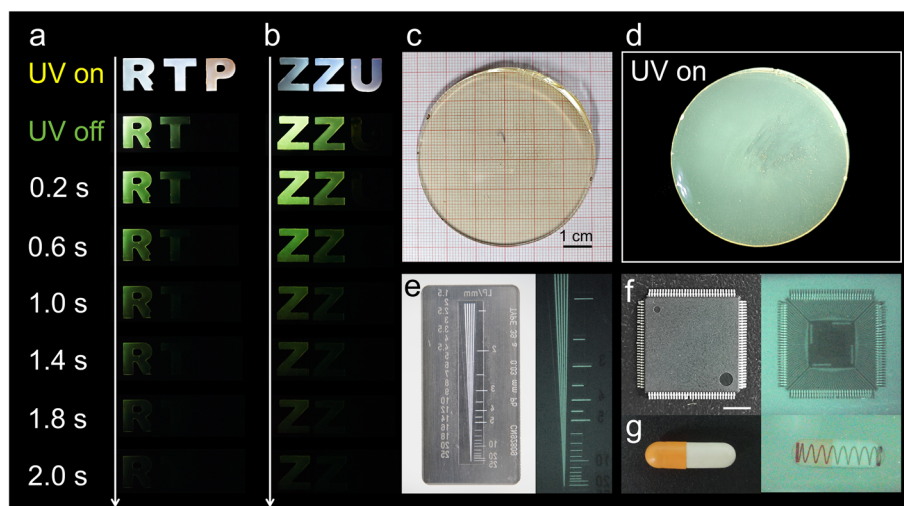

Fig. 6 Multiple anti-counterfeiting processes based on (a) "RTP" and (b) "ZZU" shaped glasses exhibiting distinct afterglow lifetimes after 365 nm UV cessation. Photographs of P-ZnI$_2$ glass scintillation screen with a diameter of 6 cm under (c) ambient light and (d) 365 nm UV light irradiation. (e) Photograph and X-ray image of a standard 25 lp mm^{-1} line pair card using P-ZnI$_2$ glass as scintillation screen. Photographs and X-ray images of a chip (f) and a capsule containing metallic spring (g) using P-ZnI$_2$ glass as scintillation screen.

emissions, while only the letter "R" remains visible after more than 1.4 s. This enables the design of customized shapes and multiple anti-counterfeiting features by selecting appropriate material combinations. A similar phenomenon is observed with the "ZZU" letter pattern (Fig. 6b), demonstrating the reproducibility and versatility of this strategy. Furthermore, by taking advantage of the facile processability, excellent glass-forming ability, and rapid emission characteristics of P-ZnI$_2$, we successfully fabricated a large-area glass scintillation screen with a diameter of 6 cm. As shown in Fig. 6c, the resulting P-ZnI$_2$ glass scintillation screen is highly transparent under ambient light and displays a uniform bright greenish white light emission under 365 nm UV irradiation (Fig. 6d). Spatial resolution, a key parameter for assessing X-ray imaging performance, was evaluated using a standard line-pair card.[48] As shown in Fig. 6e, the spatial resolution of the P-ZnI$_2$ glass scintillation screen reaches approximately 10 lp mm^{-1}, indicating good X-ray imaging capability. To demonstrate its practical applicability, a series of X-ray imaging experiments were conducted. As shown in Fig. 6f and g, fine structural details, such as the internal circuits of an electronic chip and the metallic spring inside a capsule, are clearly visible using the P-ZnI$_2$ glass scintillation screen, highlighting its strong potential for high-resolution X-ray imaging applications.[49]

Furthermore, we characterized the scintillation properties of P-ZnI$_2$ glass. Fig. S23a shows the X-ray attenuation efficiencies of P-ZnI$_2$ glass and Bi$_4$Ge$_3$O$_{12}$ (BGO) as a function of thickness at an X-ray photon energy of 22 keV, and the X-ray attenuation efficiency of BGO scintillator is superior to that of P-ZnI$_2$ glass. To accurately estimate the light yield of P-ZnI$_2$ glass, a commercial BGO scintillator (light yield: 8500 photons MeV^{-1}) was used as a reference. By calibrating the radioluminescence (RL) intensity, the light yield of P-ZnI$_2$ glass was determined to be 2296 photons MeV^{-1} (Fig. S23b). To demonstrate the linear response range to X-ray dose rates, the RL spectra of the P-ZnI$_2$ glass under various dose rates was examined. As shown in Fig. S23c, the RL intensity of P-ZnI$_2$ glass monotonically increases with dose rates ranging from 603 to 6100 µGy s^{-1}, and exhibits an excellent linear response (Fig. S23d). When the signal-to-noise ratio is 3, the linear fitting of the RL intensity yields a detection limit of 10.37 µGy s^{-1} for P-ZnI$_2$ glass (Fig. S23d). The X-ray irradiation stability of P-ZnI$_2$ glass was further examined under continuous exposure at a high dose rate of 12.7 mGy s^{-1} for 1092 s, during which the RL intensity retained over 91% of its initial value (Fig. S23e), confirming its better stability. Moreover, the RL response profile exhibited a rise time of 20 ms and a fall time of 20 ms (Fig. S23f), demonstrating prompt radiation response and rapid signal decay, both essential characteristics for practical scintillation applications. Therefore, these novel types of hybrid metal halide glasses have great potentials towards information security and X-ray imaging applications.

3 Conclusion

In conclusion, we developed a series of 0D (BuTPP)$_2$MCl$_2$X$_2$ hybrid metal halide glasses *via* a solvent-assisted rapid evaporation method, overcoming the limitations of conventional melt-quenching. The heavy-atom effect from inorganic metal halide anions [MCl$_2$X$_2$]$^{2-}$ was leveraged to systematically tune RTP lifetimes, with heavier atoms accelerating ISC and reducing phosphorescence decay lifetimes. Unique dual-mode emission, combining long-lived RTP (organic triplet states) and short-lived STE (inorganic excitons), was achieved in P-ZnI$_2$ and P-CdI$_2$ glasses. Additionally, P-ZnCl$_2$ glass displayed excitation-dependent multicolor phosphorescence, attributed to multiple aggregate cluster luminescence. The glasses' excellent processability enabled applications in shape-controlled anti-counterfeiting and X-ray imaging with high spatial resolution. This study not only advances the synthesis of hybrid metal halide glasses but also establishes a framework for designing RTP materials with programmable lifetimes and emission properties, paving the way for future optoelectronic and security technologies.

Author contributions

L. Y. L. and Z. F. S. initiated and guided the research. L. Y. L. wrote the manuscript, L. Y. L. and Z. F. S. revised it. L. Y. L. and M. A. performed material synthesis, spectra measurements, and data analysis. D. M. X., T. L., J. B. Z., M. C. J., Y. L., Z. Z. M., and X. C. assisted with luminescence properties measurements and data analysis. Y. B. Han, Y. T. T., and X. J. Li performed the X-ray scintillation properties characterization and data analysis. All authors discussed the results and commented on the manuscript.

Conflicts of interest

There are no conflicts to declare.

Data availability

The data supporting the findings of this paper are available from the corresponding author upon reasonable request.

The data supporting this article have been included as part of the supplementary information (SI). Supplementary information: experimental details, characterization data (EDS, TGA, DSC, UV-vis absorption spectra, PXRD, PL spectra, timed-resolved PL spectra, DFT calculation, temperature-dependent PL spectra, 2D GiWAXS, X-ray scintillation properties, crystal data table, and luminescence kinetic parameters table). See DOI: **https://doi.org/10.1039/d5sc06898c**.

Acknowledgements

References

1 L. Gu, H. Shi, L. Bian, M. Gu, K. Ling, X. Wang, H. Ma, S. Cai, W. Ning, L. Fu, H. Wang, S. Wang, Y. Gao, W. Yao, F. Huo, Y. Tao, Z. An, X. Liu and W. Huang, *Nat. Photonics*, 2019, **13**, 406–411.

2 L. Li, J. Zhou, J. Han, D. Liu, M. Qi, J. Xu, G. Yin and T. Chen, *Nat. Commun.*, 2024, **15**, 3846.

3 J. Wei, C. Liu, J. Duan, A. Shao, J. Li, J. Li, W. Gu, Z. Li, S. Liu, Y. Ma, W. Huang and Q. Zhao, *Nat. Commun.*, 2023, **14**, 627.

4 F. Nie and D. Yan, *Nat. Commun.*, 2024, **15**, 9491.

5 X. Wang, H. Shi, H. Ma, W. Ye, L. Song, J. Zan, X. Yao, X. Ou, G. Yang, Z. Zhao, M. Singh, C. Lin, H. Wang, W. Jia, Q. Wang, J. Zhi, C. Dong, X. Jiang, Y. Tang, X. Xie, Y. Yang, J. Wang, Q. Chen, Y. Wang, H. Yang, G. Zhang, Z. An, X. Liu and W. Huang, *Nat. Photonics*, 2021, **15**, 187–192.

6 N. Gan, X. Zou, M. Dong, Y. Wang, X. Wang, A. Lv, Z. Song, Y. Zhang, W. Gong, Z. Zhao, Z. Wang, Z. Zhou, H. Ma, X. Liu, Q. Chen, H. Shi, H. Yang, L. Gu, Z. An and W. Huang, *Nat. Commun.*, 2022, **13**, 3995.

7 M. Ren, S. Zhang, J. Wu, Q. Hu, S. Cao, B. Zou, Z. Yin, W. W. Yu and R. Zeng, *Adv. Funct. Mater.*, 2025, **35**, 2420362.

8 Y. Shen, Z. An, H. Liu, B. Yang and Y. Zhang, *Angew. Chem., Int. Ed.*, 2023, **62**, e202214483.

9 X. Li, W. Li, Z. Deng, X. Ou, F. Gao, S. He, X. Li, Z. Qiu, R. T. K. Kwok, J. Sun, D. L. Phillips, J. W. Y. Lam, Z. Guo and B. Z. Tang, *J. Am. Chem. Soc.*, 2025, **147**, 14198–14210.

10 H. Li, J. Gu, Z. Wang, J. Wang, F. He, P. Li, Y. Tao, H. Li, G. Xie, W. Huang, C. Zheng and R. Chen, *Nat. Commun.*, 2022, **13**, 429.

11 S. Feng, Q. Huang, S. Yang, Z. Lin and Q. Ling, *Chem. Sci.*, 2021, **12**, 14451–14458.

12 Z. Luo, Y. Liu, Y. Liu, C. Li, Y. Li, Q. Li, Y. Wei, L. Zhang, B. Xu, X. Chang and Z. Quan, *Adv. Mater.*, 2022, **34**, 2200607.

13 L.-J. Xu, A. Plaviak, X. Lin, M. Worku, Q. He, M. Chaaban, B. J. Kim and B. Ma, *Angew. Chem., Int. Ed.*, 2020, **59**, 23067–23071.

14 F. Nie and D. Yan, *Nat. Commun.*, 2024, **15**, 5519.

15 S. Liu, X. Fang, B. Lu and D. Yan, *Nat. Commun.*, 2020, **11**, 4649.

16 J.-Q. Zhao, D.-Y. Wang, T.-Y. Yan, Y.-F. Wu, Z.-L. Gong, Z.-W. Chen, C.-Y. Yue, D. Yan and X.-W. Lei, *Angew. Chem., Int. Ed.*, 2024, **63**, e202412350.

17 Y.-H. Liu, B.-L. Zhang, Y.-J. Wang, X.-Y. Zhang, Y.-B. Shang, T.-C. Liu, X.-W. Lei, Z.-W. Chen and C.-Y. Yue, *Adv. Opt. Mater.*, 2024, **12**, 2303285.

18 L. Zhou, K. Li, Y. Chang, Y. Yao, Y. Peng, M. Li and R. He, *Chem. Sci.*, 2024, **15**, 10046–10055.

19 Y. Peng, J. Ma, Y. Zhao, D. You, Y. Yao, Z. Deng, J. Liao, Y. Chang, W. Shen, M. Li, R. He and L. Zhou, *Adv. Funct. Mater.*, 2025, **35**, 2420311.

20 B. Li, Y. Wang, Y. Xu and Z. Xia, *Adv. Mater.*, 2025, **37**, 2415483.

21 B. Zhou and D. Yan, *Matter*, 2024, **7**, 1950–1976.

22 J.-B. Luo, J.-H. Wei, Z.-Z. Zhang, Z.-L. He and D.-B. Kuang, *Angew. Chem., Int. Ed.*, 2023, **62**, e202216504.

23 B. Zhou, Z. Qi and D. Yan, *Angew. Chem., Int. Ed.*, 2022, **61**, e202208735.

24 Z. Xu, W. Chen, K. Chen, S. Lin, Z. Wu, G. Deng, J. Chen, M. Tayyab, Y. Xiong, M.-D. Li, D. Wang, Z. An and B. Z. Tang, *Adv. Mater.*, 2025, **37**, 2418778.

25 F. Nie and D. Yan, *Sci. China Mater.*, 2024, **67**, 3531–3536.

26 B. Li, J. Jin, M. Yin, K. Han, Y. Zhang, X. Zhang, A. Zhang, Z. Xia and Y. Xu, *Chem. Sci.*, 2023, **14**, 12238–12245.

27 B. Li, J. Jin, X. Liu, M. Yin, X. Zhang, Z. Xia and Y. Xu, *ACS Mater. Lett.*, 2024, **6**, 1542–1548.

28 B. Li, J. Jin, M. Yin, X. Zhang, M. S. Molokeev, Z. Xia and Y. Xu, *Angew. Chem., Int. Ed.*, 2022, **61**, e202212741.

29 M. Yin, B. Li, Z. Yi, Y. Zhang, Z. Xia and Y. Xu, *Chem. Commun.*, 2023, **59**, 11361–11364.

30 Z.-Z. Zhang, Z.-L. He, Q.-P. Peng, J.-H. Chen, B. Lan and D.-B. Kuang, *J. Mater. Chem. C*, 2024, **12**, 17411–17418.

31 T. Wang, X. Xu, S. Yao, J. Yu, Z. Yang, J. Qiu, Y. Yang and X. Yu, *Adv. Opt. Mater.*, 2024, **12**, 2302203.

32 W. Wang, C.-D. Liu, C.-C. Fan, X.-B. Fu, C.-Q. Jing, M.-L. Jin, Y.-M. You and W. Zhang, *J. Am. Chem. Soc.*, 2024, **146**, 9272–9284.

33 X. Li, Y. Yang, Z. Zhao, S. Bai, Q. Li and J. Li, *Angew. Chem., Int. Ed.*, 2025, **64**, e202422272.

34 R. Zhang, H. Xie, W. Liu, K. Zhan, H. Liu, Z. Tang and C. Yang, *ACS Appl. Mater. Interfaces*, 2023, **15**, 47238–47249.

35 Y. Xu, Z. Li, C. Shi, Y. Li, Y. Lei, G. Peng, T. Yu, H. Ren, H. Wang, H. Fan, Y. Zhang, Z. Ci, Q. Wang and Z. Jin, *Adv. Mater.*, 2024, **36**, 2406128.

36 S. Zaghden, H. Ben Attia, M. S. M. Abdelbaky, A. Oueslati, S. García-Granda, M. Dammak and L. Ktari, *ACS Omega*, 2024, **9**, 47597–47612.

37 G. Zhou, Y. Mao, J. Zhang, Q. Ren, M. S. Molokeev, Z. Xia and X.-M. Zhang, *Adv. Funct. Mater.*, 2025, **35**, 2413524.

38 L. Lian, D. Xiong, J. Zhang, M. Jia, Y. Liu, Z. Ma, X. Chen, Y. Han, Y. Tian, X. Li, J. Zhang and Z. Shi, *Laser Photonics Rev.*, 2025, e00509.

39 Z.-Y. Li, R. Feng, S.-S. Huang, W. Li and X.-H. Bu, *J. Am. Chem. Soc.*, 2025, **147**, 7017–7027.

40 L. Lian, M. Zheng, P. Zhang, Z. Zheng, K. Du, W. Lei, J. Gao, G. Niu, D. Zhang, T. Zhai, S. Jin, J. Tang, X. Zhang and J. Zhang, *Chem. Mater.*, 2020, **32**, 3462–3468.

41 L. Lian, P. Zhang, G. Liang, Y. Xia, J. Gao, D. Zhang and J. Zhang, *ACS Appl. Mater. Interfaces*, 2024, **16**, 9030–9038.

42 L. Lian, X. Wang, P. Zhang, J. Zhu, X. Zhang, J. Gao, S. Wang, G. Liang, D. Zhang, L. Gao, H. Song, R. Chen, X. Lan, W. Liang, G. Niu, J. Tang and J. Zhang, *J. Phys. Chem. Lett.*, 2021, **12**, 6919–6926.

43 L. Lian, M. Zheng, W. Zhang, L. Yin, X. Du, P. Zhang, X. Zhang, J. Gao, D. Zhang, L. Gao, G. Niu, H. Song,

R. Chen, X. Lan, J. Tang and J. Zhang, *Adv. Sci.*, 2020, **7**, 2000195.

44 L. Kang, J. Xu, J. Wu, Q. Ling and Z. Lin, *Inorg. Chem. Front.*, 2025, **12**, 5133–5142.

45 L. Hou, T. Wang, S. Yu, X. Xu and X. Yu, *Aggregate*, 2025, **6**, e70071.

46 J. Zhang, Z. Xiong, H. Zhang and B. Z. Tang, *Nat. Commun.*, 2025, **16**, 3910.

47 H. Wang, H. Shi, W. Ye, X. Yao, Q. Wang, C. Dong, W. Jia, H. Ma, S. Cai, K. Huang, L. Fu, Y. Zhang, J. Zhi, L. Gu, Y. Zhao, Z. An and W. Huang, *Angew. Chem., Int. Ed.*, 2019, **58**, 18776–18782.

48 L. Lian, D. Xiong, J. Zhang, M. Jia, Y. Liu, Z. Ma, X. Chen, Y. Han, Y. Tian, X. Li, J. Zhang, S. Qian, C. Shan and Z. Shi, *Appl. Phys. Rev.*, 2025, **12**, 031409.

49 L. Lian, D. Xiong, J. Zhang, M. Jia, Y. Liu, Z. Ma, X. Chen, Y. Han, Y. Tian, X. Li, J. Zhang, P. Zhang and Z. Shi, *Laser Photonics Rev.*, 2025, e01538.